International Journal of Heat and Mass Transfer 52 (2009) 2444–2452

Contents lists available at ScienceDirect

International Journal of Heat and Mass Transfer

journal homepage: www.elsevier.com/locate/ijhmt

An ablation model for the thermal decomposition of porous zinc oxide layer heated by concentrated solar radiation

Leonid Dombrovsky [a,*], Lothar Schunk [b], Wojciech Lipiński [c], Aldo Steinfeld [b,d]

[a] Joint Institute for High Temperatures of the Russian Academy of Sciences, Krasnokazarmennaya 17A, NCHMT, Moscow 111116, Russia
[b] Solar Process Technology, Paul Scherrer Institute, CH-5232 Villigen, Switzerland
[c] Department of Mechanical Engineering, University of Minnesota, Minneapolis, MN 55455, USA
[d] Department of Mechanical and Process Engineering, ETH Zurich, 8092 Zurich, Switzerland

ARTICLE INFO

Article history:
Received 18 November 2008
Received in revised form 22 December 2008
Available online 27 February 2009

Keywords:
Thermal decomposition
Zinc oxide
Kinetics
Heat transfer
Semi-transparent
Solar energy

ABSTRACT

Thermal decomposition of porous ZnO under high-flux solar irradiation is considered. The process is well described by a transient ablation model that couples radiation, conduction, and convection heat transfer to an Arrhenius-type kinetic rate law with a pre-exponential factor dependent on the porosity, grain/pore size, and convective removal of the reaction products Zn(g) and O_2. Main model parameters are determined by comparing numerical and experimental results.

1. Introduction

Solar thermochemical processes make use of concentrated solar radiation as the energy source of high-temperature process heat [1,2]. Examples are the thermal decomposition of limestone [3], the thermal reduction of metal oxides [4], the thermal cracking of natural gas [5], and the thermal gasification of carbonaceous materials [6]. Of particular interest is the production of hydrogen by the 2-step water-splitting chemical cycle via ZnO/Zn redox reactions [4]:

1st step (solar, endothermic):

$$ZnO \rightarrow Zn + 0.5O_2 \quad (1)$$

2nd step (non-solar, exothermic):

$$Zn + H_2O \rightarrow ZnO + H_2 \quad (2)$$

H_2 and O_2 are formed in separate steps, eliminating the need for high-temperature gas separation. This cycle has been identified as a promising path for solar hydrogen production because of its potential of reaching high energy conversion efficiencies and, consequently, of economic competitiveness [4,7].

The physical analysis of thermal processes in the reactor and the choice of suitable engineering solutions require a complete model linking the rate of heat transfer to that of the chemical reaction. The experimental work on the dissociation of ZnO has been reported in several papers [8–10]. An early study by Secco [11] indicated a strong dependence of the mass loss of pure polycrystalline ZnO on the sample temperature, composition, and pressure. The reaction rate was about an order of magnitude lower at 1 bar Ar than in vacuum. Hirschwald and Stolze [12] found that the ZnO decomposition in the range 1130–1385 K in vacuum was well described by the Arrhenius-type law with activation energy $E = 327.3$ kJ mol^{-1}. A comparable value of E was found for ZnO powder heated by thermal radiation [12]. However, the pre-exponential factor depended strongly on the sample structure: it was twice and five times larger for the sintered and powdery samples than for the crystals, respectively. ZnO evaporation from spinel solid solutions in vacuum revealed rate limiting mechanisms controlled by chemical decomposition and diffusion [13]. Möller and Palumbo [14] investigated the decomposition of sintered ZnO samples exposed to concentrated solar radiation in Ar filled volume at atmospheric pressure and determined an Arrhenius-type rate law in the range 1950–2400 K with $E = 328.5$ kJ mol^{-1}. Although the value of E was comparable to that obtained under vacuum conditions [12], the rate in Ar was 30 times slower than in vacuum. In a follow-up study, the effect of sintering and shrinkage on the rate of heat transfer was examined for a packed-bed of ZnO particles subjected to solar flux concentration ratios in the range 1225–2133 suns and surface temperatures in the range 1834–2109 K [15,16].

The ZnO decomposition rate is strongly influenced by the sample structure, and may be considerably higher for porous

* Corresponding author. Tel.: +7 495 362 5590/250 3264; fax: +7 495 362 5590.
E-mail address: dombr@online.ru (L. Dombrovsky).

0017-9310/$ - see front matter © 2009 Elsevier Ltd. All rights reserved.
doi:10.1016/j.ijheatmasstransfer.2008.12.025

Nomenclature

a	particle radius, m
A	coefficient in Eq. (28)
B_λ	blackbody radiation intensity (Plank function), W m^{-3}
c	specific heat capacity, J kg^{-1} K^{-1}
d	sample thickness, m
D	radiation diffusion coefficient, m
E	activation energy, J mol^{-1}
F_v	volume distribution function of particles, m^{-1}
H	specific enthalpy, J kg^{-1}
H_0	formation enthalpy, J kg^{-1}
I_λ^0	spectral radiation energy density, W m^{-3}
k	thermal conductivity, W m^{-1} K^{-1}
K	pre-exponential factor, kg m^{-2} s^{-1}
n	index of refraction; external normal
$\dot{m}$	decomposition rate, kg m^{-2} s^{-1}
p	porosity
q	heat flux, W m^{-2}
Q_s^{tr}	transport efficiency factor of scattering
r	radial coordinate, m
R	universal gas constant J mol^{-1} K^{-1}
s	scaling factor
S	irradiated sample surface
t	time, s
T	temperature, K
y	internal normal coordinate, m

Greek symbols

α	absorption coefficient, m^{-1}
α_s	absorptivity of solar radiation
β	extinction coefficient, m^{-1}
δ	thickness of ceramic tube, m
ε	emissivity
ρ	density, kg m^{-3}
σ	Stefan–Boltzmann constant, W m^{-2} K^{-4}
σ^{tr}	transport scattering coefficient, m^{-1}
κ	index of absorption
λ	wavelength, m
ν	stoichiometric coefficient

Subscripts

c	ceramics
p	at constant pressure
p	plate
p_1, p_2	measurement points
r	radiative
R	Rosseland
s	solar, sample
tr	transport
v	volume
w	wall
λ	spectral
0	initial

Overbar

$\bar{}$	dimensionless quantity

samples with rough surface and open pores. In the present study, the applicability of the surface ablation model for porous samples prepared from various ZnO powders is analyzed based on the experimental data. A heat transfer model is developed and the main physical characteristics are estimated by use of detailed temperature and mass loss measurements. The model includes two-dimensional conduction heat transfer in the sample and insulation, volumetric effects of thermal radiation, convective heat transfer between the sample and the ambient gas, and radiative exchange between the sample and the walls of the thermogravimeter cavity. Finally, the effects of varying the Ar mass flow rate on the removal of gaseous products are discussed.

2. Experimental procedure and typical experimental results

The experimental set-up and methodology have been described in detail [15,16]; only the main features are summarized here and shown schematically in Fig. 1. The solar-driven thermogravimeter (solar TG), shown in Fig. 1a, consists of a well-insulated cylindrical cavity of 152 mm i.d. and 150 mm length, lined with 50 mm-thick CaO-stabilized ZrO_2 bricks over two layers of 36 mm-thick porous Al_2O_3. It has a 60 mm-diameter aperture to let in concentrated solar energy through a transparent 3 mm-thick quartz window. Inside the cavity, the ZnO sample is mounted on an Al_2O_3 rod that is suspended on a balance (Mettler Toledo; accuracy 0.01 g). With this arrangement, the ZnO sample is directly exposed to concentrated solar radiation while its weight loss during decomposition is continuously monitored. An Ar flow, injected tangentially and radially at the aperture plane, carries the gaseous products Zn(g) and O_2 to the outlet port at the rear of the cavity. Ar gas is also introduced into the box containing the balance to prevent back-flow of hot gases. Downstream, the Zn(g) is condensed and filtered, and the gas composition is analyzed. Experimentation was carried out at PSI's solar furnace [17]: a sun-tracking flat heliostat on-axis with a stationary primary paraboloidal concentrator. Peak solar radiative flux intensities exceeding 5000 kW m^{-2} are achieved, enabling the sample in the solar TG to attain temperature above 2500 K at heating rates higher than 1000 K/s. Solar flux intensities, regulated with a Venetian-type shutter located between the heliostat and the solar concentrator, are measured optically with a calibrated CCD camera on a water-cooled Al_2O_3-plasma coated Lambertian target.

Samples of ZnO were placed in cylindrical Al_2O_3 CMC tubular containers and exposed to concentrated solar irradiation. In this study, two sample configurations were used, as shown schematically in Fig. 1b and c. Sample #1 (Fig. 1b) consisted of a 12 mm-thick porous ZnO powder layer, followed by a 3.7 mm-thick sintered ZnO tile and 24.3 mm-thick 80% Al_2O_3–20% SiO_2 porous insulation. Sample #2 consisted of two sintered plates of thickness 3.7 mm each and ZnO powder layer of thickness 12 mm between the plates. The temperature of the irradiated front surface of the sample, T_S, was measured with the solar-blind pyrometer (measurement range 773–2773 K) that is not affected by the reflected solar irradiation because it measures in a narrow wavelength interval around 1.39 μm where solar irradiation is mostly absorbed by the water vapor in the atmosphere. The temperatures T_{p_1}, T_{p_2}, and T_c were measured with type-B thermocouples. Sample mass was instantaneously acquired by the mass balance.

Particle volume distribution functions for two ZnO powders used in the experiments, $F_{v,1}$ and $F_{v,2}$, respectively, are shown in Fig. 2. The corresponding mean particle radii, calculated as

$$a_{ij} = \int_0^\infty a^{i-3} F_v(a)\mathrm{d}a \Big/ \int_0^\infty a^{j-3} F_v(a)\mathrm{d}a \tag{3}$$

are $a_{32,1}$ = 0.96 μm and $a_{32,2}$ = 3.14 μm.

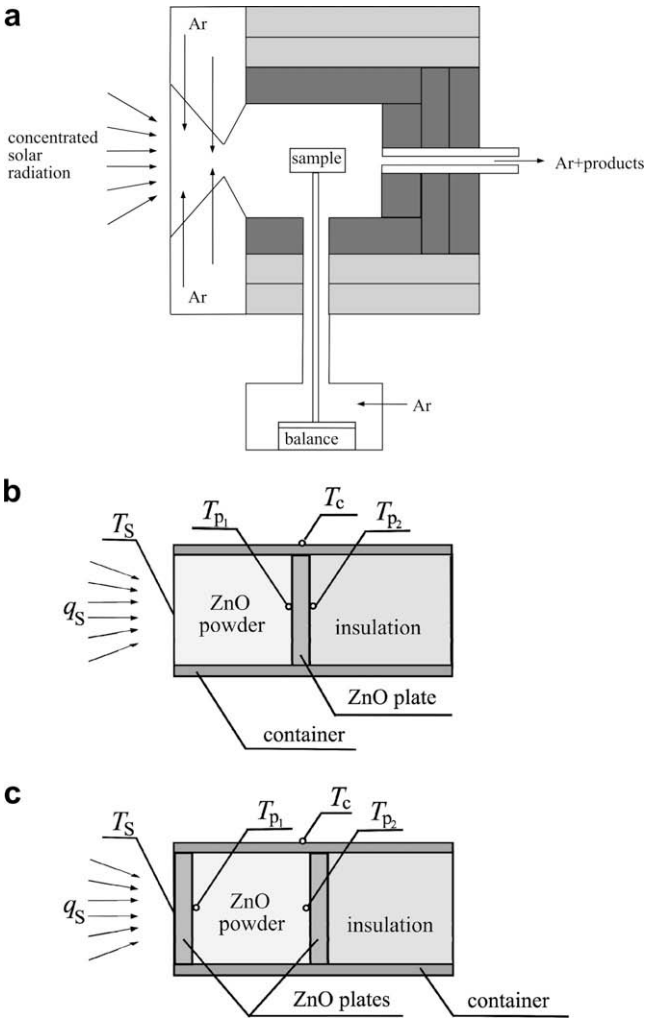

Fig. 1. Experimental set-up: (a) schematic of the solar TG [15], (b) sample #1, (c) sample #2. Indicated are temperature measurement points by type-B thermocouples, T_{p_1}, T_{p_2}, and T_c, and by a solar-blind pyrometer, T_S, respectively.

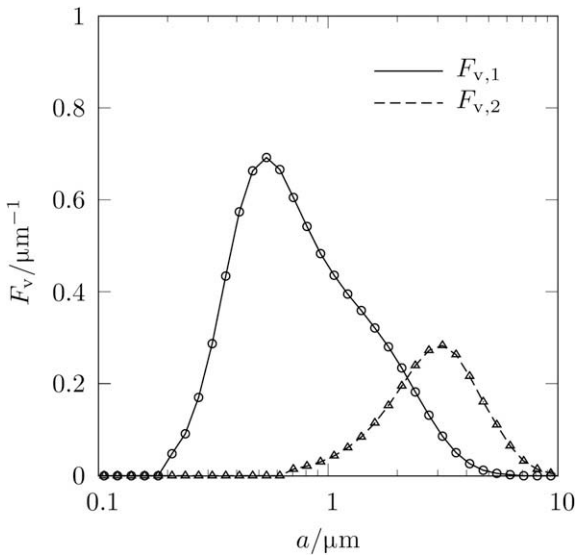

Fig. 2. Volume distribution function of ZnO particles for two powders used for the preparation of porous samples.

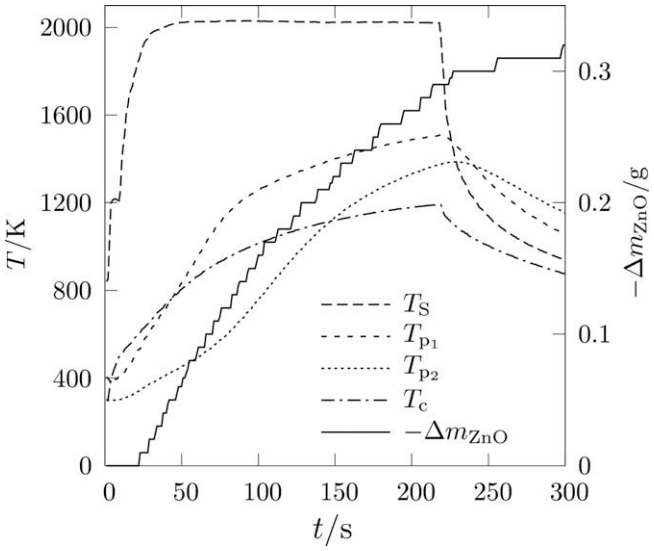

Fig. 3. Experimentally measured temperatures and mass loss profiles as a function of time during a representative solar run.

Typical experimental results obtained with sample #1 are shown in Fig. 3. A strong correlation between the temperature of the irradiated surface of the sample and the mass loss rate of ZnO is observed. Therefore, it is assumed that surface ablation is of primary importance in the decomposition mechanism of porous ZnO while the volumetric effects of both the decomposition of porous ZnO and combined heat transfer inside the sample play secondary role. This hypothesis is anticipated to be specific for the experiments conducted in the solar TG. The conditions in a real solar reactor may differ from those in the present experiments and volumetric effects may contribute more to the decomposition process, in particular due to a more pronounced role of infrared radiation emitted within the reactor cavity. Fig. 4 shows photographs of the front surface of a non-pre-sintered sample (4a) and a pre-sintered sample (4b) after the experiment. The formation of the needle-like structures on both samples was described by numerous authors [18–21] and is attributed to Zn vapor phase deposition followed by re-oxidation and crystallization. This in turn supports the hypothesis of the predominant role of surface processes and the use of an approximate ablation model. The sample in Fig. 4a revealed fractures due to thermal stresses during the rapid radiative heating, while no cracks were observed in the pre-sintered ZnO plate of Fig. 4b.

3. Theoretical model of surface ablation and combined heat transfer in the sample

Conduction and thermal radiation in the porous ZnO sample are modeled by using average transport properties estimated from the experimental data such as temperature profiles and mass losses. The energy conservation equation for a semi-transparent material is given by

$$\rho c \frac{\partial T}{\partial t} = \nabla(k \nabla T) - \nabla \cdot \vec{q}_r \tag{4}$$

where $\vec{q}_r$ is the total radiative flux. It is assumed here that the dissociation reaction is occurring only at the top (irradiated) thin layer of the sample because of: (i) a very low porosity of ZnO at high temperatures, leading to high resistance to gas diffusion and consequently inhibition of the reaction behind the reacting surface layer [14] and (ii) a strong dependence of the rate of ZnO

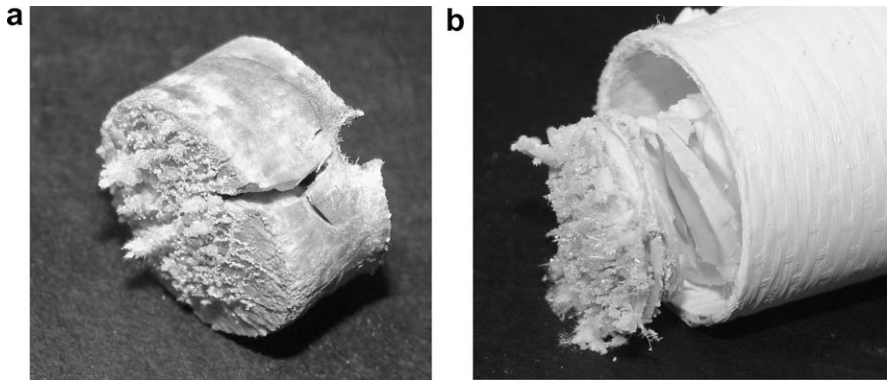

Fig. 4. Photographs of samples taken after the solar runs: (a) porous ZnO sample, and (b) pre-sintered ZnO sample.

dissociation on temperature according to the Arrhenius law. Thus, the enthalpy change of the reaction is not included as the source term in Eq. (4), but in its boundary condition.

Two spectral ranges of thermal radiation are of special interest: (i) the visible range (VR), covering most of the external solar radiation, and (ii) the near infrared range (NIR), covering most of the radiation emitted by the sample. The optical properties of ZnO are significantly different in these two ranges. In VR, the absorption coefficient is several orders of magnitude larger than that in NIR, and the material is practically opaque for solar radiation but is semi-transparent for the thermal radiation emitted by the sample (see also Section 4). Therefore, the external solar flux can be included in the boundary condition of the energy Eq. (4) at the illuminated surface S, whereas the infrared radiation constitutes the divergence of radiative flux $\vec{q}_r$ in Eq. (4). Porous materials are usually characterized by strong scattering and large optical thickness even for small geometrical thickness of the sample. Preliminary calculations showed that this applies to the samples used in the present study. Thus, P_1 approximation can be employed to model the NIR radiative transfer in the sample [22,23]. The resulting equations can be written as follows:

$$\rho c\frac{\partial T}{\partial t}=\nabla(k\nabla T)-\int_{\lambda_1}^{\lambda_2}\alpha_\lambda\left[4\pi n_\lambda^2 B_\lambda(T)-I_\lambda^0\right]\mathrm{d}\lambda \tag{5}$$

$$t=0\quad T=T_0 \tag{6}$$

$$-k\frac{\partial T}{\partial n}=h(T-T_g)-\alpha_s q_s+\dot{m}\Delta H \text{ at surface } S \tag{7}$$

$$-k\frac{\partial T}{\partial n}=h(T-T_g)+\varepsilon_c\sigma\left(T^4-T_w^4\right) \text{ at other surfaces} \tag{8}$$

$$-\nabla\left(D_\lambda\nabla I_\lambda^0\right)+\alpha_\lambda I_\lambda^0=\alpha_\lambda 4\pi n_\lambda^2 B_\lambda(T) \tag{9}$$

$$-D_\lambda\frac{\partial I_\lambda^0}{\partial n}=\frac{\gamma_w}{2}\left[4\pi n_\lambda^2 B_\lambda(T_w)-I_\lambda^0\right]\quad \gamma_w=\frac{\varepsilon_w}{2-\varepsilon_w} \text{ at surface } S \tag{10}$$

$$-D_\lambda\frac{\partial I_\lambda^0}{\partial n}=\frac{\gamma_c}{2}\left[4\pi n_\lambda^2 B_\lambda(T)-I_\lambda^0\right]\quad \gamma_c=\frac{\varepsilon_c}{2-\varepsilon_c} \text{ at other surfaces} \tag{11}$$

where the radiation diffusion coefficient is given by

$$D_\lambda=\frac{1}{3\beta_\lambda^{tr}}\quad \beta_\lambda^{tr}=\alpha_\lambda+\sigma_\lambda^{tr} \tag{12}$$

α_λ and σ_λ^{tr} are the absorption and transport scattering coefficients, respectively [22]. Eqs. (9)–(11) are valid for the complete computational region including the ceramic insulation, which is semi-transparent in NIR, $\lambda_1<\lambda<\lambda_2$. Note that the factor n_λ^2 has to be omitted for a highly porous medium consisting of hot grains immersed in a non-refractive host medium. The velocity and the actual position of the irradiated surface S are determined by the rate of surface ablation,

$$\frac{\mathrm{d}y}{\mathrm{d}t}=\frac{\dot{m}}{\rho}\dot{m}=K\exp\left(-\frac{E}{RT}\right) \tag{13}$$

where y is the local coordinate measured along the normal vector pointing from S into the sample interior, $\dot{m}$ is the local decomposition rate, and E is the activation energy of endothermic decomposition. Eqs. (5)–(12) can be further simplified by assuming that D_λ is low and n_λ is constant. In this case, the Rosseland diffusion approximation for the total radiative flux can be applied [23]:

$$\vec{q}_r=-k_r\nabla T\quad k_r=16D_R n^2\sigma T^3 \tag{14}$$

where the Rosseland-averaged radiation diffusion coefficient is given by

$$D_R=\int_{\lambda_1}^{\lambda_2}D_\lambda\frac{\partial B_\lambda(T)}{\partial T}\mathrm{d}\lambda\Big/\int_{\lambda_1}^{\lambda_2}\frac{\partial B_\lambda(T)}{\partial T}\mathrm{d}\lambda \tag{15}$$

The Rosseland approximation accurately predicts radiative flux inside a medium at large optical distance from the sample boundaries but it fails near the boundaries [22,23]. Therefore, the following combined model is proposed:

$$\rho c\frac{\partial T}{\partial t}=\nabla(k_*\nabla T)\quad k_*=k+k_r \tag{16}$$

$$t=0\quad T=T_0 \tag{17}$$

$$-k_*\frac{\partial T}{\partial n}=h(T-T_g)+\varepsilon\sigma\left(T^4-T_w^4\right)-\alpha_s q_s+\dot{m}\Delta H \text{ at surface } S \tag{18}$$

$$-k\frac{\partial T}{\partial n}=h(T-T_g)+\varepsilon_c\sigma\left(T^4-T_w^4\right) \text{ at other surfaces} \tag{19}$$

Simple estimates showed that convective heat flux at the surface S is much smaller than the incident solar flux or the flux emitted by the sample. At the same time, the quasi-steady temperature field in the sample depends considerably on convective heat losses from the cylindrical sample container. Therefore, the heat transfer coefficient h is calculated as an average value around the horizontal cylinder by using the natural convection correlation by Churchill and Chu [24]. For simplicity, the same approximate value is used for all surfaces around the computational region. The small contribution by forced convection due to Ar flow is neglected.

The enthalpy of the endothermic ZnO dissociation reaction is given by:

$$\Delta H(T)=\sum_i \nu_i\left(H_{0,i}+\int_{T_{ref}}^{T}c_{p,i}\mathrm{d}T\right) \tag{20}$$

where i = ZnO, Zn, and O_2. Formation enthalpies $H_{0,i}$ and the specific heats $c_{p,i}$ are taken from [25]. The resulting $\Delta H(T)$ is monotonically decreasing from 5.74 MJ kg^{-1} at 1500 K to 5.49 MJ kg^{-1} at 2500 K.

The system of Eqs. (16)–(20) is used to compute the transient temperature field in the sample. However, it contains several unknown coefficients describing the material physical properties. Those of them that could not be indentified based on the solar TG experimental data were determined independently as presented in the next section.

4. Physical properties of porous zinc oxide

4.1. Density

The density of the bulk ZnO is assumed to be constant, $\rho = 5600\ \mathrm{kg\ m^{-3}}$. The density of the porous material is $(1-p)\rho$, where p is the material porosity. Note that p changes significantly during an experimental run due to sintering [16,18,19].

4.2. Thermal conductivity

A monotonically decreasing value from $k = 30\ \mathrm{W\ m^{-1}\ K^{-1}}$ at 298 K to about $k = 3.5\ \mathrm{W\ m^{-1}\ K^{-1}}$ at 1100 K is reported in [26]. Similar values were measured recently by Cai et al. [27] for hot-pressed ceramic samples of fine ZnO powder (particles of size 1.1–2 μm). It was found that k decreases from about $28.5\ \mathrm{W\ m^{-1}\ K^{-1}}$ at 298 K to $8\ \mathrm{W\ m^{-1}\ K^{-1}}$ at 873 K. The dependence of the thermal conductivity on an average particle diameter from $0.745\ \mathrm{W\ m^{-1}\ K^{-1}}$ at the particle diameter 1 μm to $1.16\ \mathrm{W\ m^{-1}\ K^{-1}}$ at 0.02 μm was found by Olorunyolemi et al. [28]. These values increase with temperature up to $1.1–2\ \mathrm{W\ m^{-1}\ K^{-1}}$ at 873 K, whereas the maximum is reached for the smallest particles. Moreover, it was shown experimentally and verified theoretically that k increases not only during heating but also during a subsequent cooling, leading to a value of $2.6\ \mathrm{W\ m^{-1}\ K^{-1}}$ at 298 K for the initial average particle diameter of 1 μm. Thermal conductivity of a fully sintered sample is given in [22]. It decreases from 37 W m^{-1} K^{-}1 at 298 K to $4\ \mathrm{W\ m^{-1}\ K^{-1}}$ at 1273 K. To our best knowledge, there are no data on thermal conductivity for ZnO in the temperature range 1300–2300 K. Based on the data from [26], k is assumed to decrease below $4\ \mathrm{W\ m^{-1}\ K^{-1}}$ at above 1300 K.

4.3. Optical constants

The index of refraction of ZnO is widely available in the literature [29–32]. Its spectral variation in the visible and near infrared spectral ranges is small and one can use the constant value $n = 1.9$. At the same time, the absorption index in the semi-transparency range is only partially known. Following the approximation used in [33,34], it can be expressed as

$$\kappa_\lambda = \begin{cases} \kappa_0, & \lambda < \lambda_0 \\ \kappa_1 + (\kappa_0 - \kappa_1)/\left[1 + \gamma(\lambda^2 - \lambda_0^2)\right], & \lambda > \lambda_0 \end{cases} \tag{21}$$

where $\kappa_0 = 0.5$, $\lambda_0 = 0.37\ \mu\mathrm{m}$, $\gamma = 120\ \mu\mathrm{m^{-2}}$ and $10^{-4} < \kappa_1 = 5 \times 10^{-4}$. Eq. (21) approximates the data by Yoshikawa and Adachi [31] in VIR ($\lambda < 0.8\ \mu\mathrm{m}$) and is only a formal extrapolation to NIR. Additional information on the ZnO absorption index in NIR can be extracted from the experiments by Tolksdorf [35]. The value of $\kappa_\lambda = 5.8 \times 10^{-4}$ for $\lambda > 4.02\ \mu\mathrm{m}$, calculated from the reported transmittance of $T_\lambda = 53.8\%$ of ZnO crystal sample of thickness $d = 2$ mm, is in a good agreement with approximation (21). Bogner and Mollwo [36] found that small additives of copper or indium to pure crystal of ZnO significantly increased the absorption index in the wavelength range 0.4–10 μm. Thomas [37] measured absorption of single ZnO crystals in the 1–12 μm range. Most results were obtained at room temperature with the crystals surrounded by air. A lithium-doped crystal, virtually free of conduction electrons, showed no absorption between the intrinsic absorption near 0.4 μm and the infrared lattice absorption bands with peaks at 10.1 and 11.5 μm. For an undopted crystal, absorption is appreciable and increases for wavelengths greater than 2 μm, but only small absorption maxima and minima can be observed for wavelengths smaller than those corresponding to the lattice bands. The reported absorption coefficient at $\lambda = 4\ \mu\mathrm{m}$ is approximately $\alpha_\lambda = 20\ \mathrm{cm^{-1}}$, which corresponds to $\kappa_\lambda = 6.4 \times 10^{-4}$. Recent studies confirm high transparency of the films of pure ZnO in the range 0.5–2.3 μm [38–40]. An absorption peak due to admixtures containing O–H bonds at $\lambda \approx 3\ \mu\mathrm{m}$ was observed by Keyes et al. [39]. Shiraka et al. [40] showed that the presence of oxygen flow during the manufacturing process of polycrystalline Ga-doped ZnO films of an average thickness of 0.18 μm increases their absorption coefficient in the near-infrared range.

4.4. Radiative properties

The radiative properties of porous materials depend on the spectral optical constants of solid grains, the porosity p, and material structure characterized by several parameters including the characteristic pore/grain size. The determination of the absorption, transport scattering, and transport extinction coefficients, α_λ, $\sigma_\lambda^{\mathrm{tr}}$, and $\beta_\lambda^{\mathrm{tr}}$, respectively, of a porous material directly from its bulk optical constants and the structural characteristics is a complex problem even in a relatively simple case of large pores and particles when geometrical optics approximation is applicable [41,42]. In the case of small particles of size comparable with radiation wavelength, the radiative properties are usually determined experimentally. α_λ and $\beta_\lambda^{\mathrm{tr}}$ can be identified on the basis of spectral measurements of directional-hemispherical reflectance and transmittance of thin plane-parallel samples [43–46]. For ZnO, the specific character of the optical properties enables one to introduce several simplifications in the semi-transparency range. The absorption coefficient of a weakly absorbing porous material is proportional to the material density:

$$\alpha_\lambda = (1-p)\alpha_{\lambda 0} \tag{22}$$

where $\alpha_{\lambda 0} = 4\pi\kappa_\lambda/\lambda$ is the absorption coefficient of the bulk material. This approximation was recently confirmed to be applicable for semi-transparent ZrO ceramics [44]. The transport scattering coefficient of porous materials can be estimated by using the following relations [22,43]:

$$\sigma_\lambda^{\mathrm{tr}} = 0.75 s \frac{1-p}{a_{32}} \overline{Q}_s^{\mathrm{tr}} \quad \overline{Q}_s^{\mathrm{tr}} = \int_0^\infty Q_s^{\mathrm{tr}} a^{-1} F_v(a)\mathrm{d}a \Big/ \int_0^\infty a^{-1} F_v(a)\mathrm{d}a \tag{23}$$

where Q_s^{tr} is the transport efficiency factor of scattering of single particles, a_{32} is the characteristic size of spherical grains, s is the scaling factor taking into account the dependent scattering effects. Singh and Kaviany [47,48] proposed an analytical expression for $s(p)$ for emitting, highly-absorbing beds of large spherical particles for $p > 0.3$. An alternative relation, $s = 1/p$, was derived by Brewster [49] by using the mean-beam-length approach for packed beds of large opaque spheres. The values predicted by this relation for $p > 0.3$ are in good agreement with those obtained by a Monte Carlo simulation by Singh and Kaviany and, more recently, by Coquard and Baillis [50]. Although the particles used in the present study are mostly of size comparable with radiation wavelength are semi-transparent, we use Eq. (23) with the scaling factor $s = 1/p$ for very preliminary estimates of $\sigma_\lambda^{\mathrm{tr}}$. Application of the Mie theory to the ZnO particles with size distributions shown in Fig. 2 leads to $\sigma_\lambda^{\mathrm{tr}}$ between 250 and 600 $\mathrm{mm^{-1}}$ for distribution $F_{\mathrm{v},1}$ and between 50 and 150 $\mathrm{mm^{-1}}$ for distribution $F_{\mathrm{v},2}$, respectively, in the wavelength range from $\lambda_1 = 0.8\ \mu\mathrm{m}$ to $\lambda_2 = 4\ \mu\mathrm{m}$, and for $p = 0.71$ (the same initial porosity for both size distributions). The real grains in a sample

may be larger than single primary ZnO particles due to agglomeration and subsequent sintering at high temperatures, but scattering is anticipated to remain the dominant attenuation mode of radiation including NIR. Finally, the spectral emissivity of a porous weakly-absorbing material can be estimated as [22]:

$$\varepsilon_\lambda = \frac{2\sqrt{\alpha_\lambda/\beta_\lambda^{tr}}}{1+\sqrt{\alpha_\lambda/\beta_\lambda^{tr}}} \tag{24}$$

According to Eq. (24), the emissivity of porous ZnO material decreases monotonically with wavelength because of a similar trend of the absorption coefficient. This prediction is in good qualitative agreement with experimental data by Möller [51].

5. Analysis

5.1. Estimation of thermal conductivity of sintered ZnO plate from the measured temperatures

Thermal conductivity of sintered ZnO is determined based on temperature profiles measured during a cooling phase of the experiment with sample #1 (Fig. 1b). A small difference between temperatures T_{p_1} and T_{p_2}, shows that heat is transferred mainly into the radial direction, i.e. through the wall of ceramic tube to ambient gas. A simultaneous measurement of the tube surface temperature T_c enables verification of both the thermal conductivity of the ZnO plate and the heat flux at the tube surface. Consider the following transient problem for radial heat conduction in the plate and the tube:

$$\rho c\frac{\partial T}{\partial t} = \frac{1}{r}\frac{\partial}{\partial r}\left(kr\frac{\partial T}{\partial r}\right) \tag{25}$$

$$t = 0 \quad T = T_0(r) \tag{26}$$

$$r = 0\frac{\partial T}{\partial r} = 0 \quad r = r_0 = r_s + \delta T = T_c(t) \tag{27}$$

where r_s and δ are the plate radius and tube thickness, respectively. Assuming constant thermal properties, the following approximation is employed for the initial radial temperature profile (see also [34]):

$$T_0(r) = \begin{cases} T_{p,0} - A(r/r_s)^2, & 0 < r < r_s \\ T_{c,0} + 2A\bar{k}(r_0 - r)/r_s, & r_s < r < r_0 \end{cases} \tag{28}$$

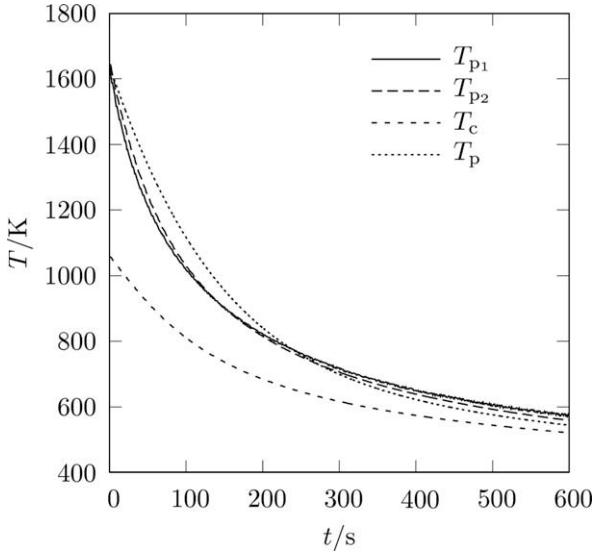

Fig. 5. Temperature of sintered ZnO plate center and ceramic tube surface after the active phase of experiment: T_{p_1}, T_{p_2}, T_c – measured, T_p – numerically calculated at the plate center.

where

$$T_{p,0} = \frac{T_{p_1}(0) + T_{p_2}(0)}{2} \quad T_{c,0} = T_c(0) \quad A = \frac{T_{p,0} - T_{c,0}}{1 + 2\bar{\delta}\bar{k}}$$

$$\bar{\delta} = \frac{\delta}{r_s} \quad \bar{k} = \frac{k_{ZnO}}{k_c} \tag{29}$$

The calculations were performed for $(\rho c)_{ZnO} = 2.8$ MJ m^{-3}, $(\rho c)_c = 0.32$ MJ m^{-3}, $k_c = 0.25$ W m^{-1} K^{-1} and $k_{ZnO} = 2$ W m^{-1} K^{-1}. The resulting temperature profiles at various times are similar to the initial temperature profile, corroborating the correct choice of the latter. Also, the transient temperature at the center of the plate, $T_p(t) = T(t,0)$, is in fairly good agreement with that obtained experimentally as shown in Fig. 5. Additional calculations for $k_{ZnO} = 1$ and 3 W m^{-1} K^{-1} confirmed the value of $k_{ZnO} = 2$ W m^{-1} K^{-1} to be a good choice in the temperature range 600–1600 K.

5.2. Estimation of the heat flux at the lateral wall of the sample container

It is necessary to validate the boundary condition at the lateral wall before it is employed in the complete computational model. The heat flux from the lateral surface of the sample container can be estimated without heat conduction calculations because one can use a parabolic approximation of the temperature profile similar to Eq. (28). The resulting heat flux is given by

$$q(t) = \frac{k_1}{r_s}\frac{T_{p,1}(t) + T_{p,2}(t) - 2T_c(t)}{1 + 2\bar{\delta}\bar{k}} \tag{30}$$

The results of calculations based on Eq. (30) are in good agreement with those based on the convection–radiation boundary condition,

$$q(t) = h[T_c(t) - T_g] + \varepsilon_c\sigma\left[T_c^4(t) - T_w^4(t)\right] \tag{31}$$

where $T_g = 300$ K and $\varepsilon_c = 0.85$. The heat transfer coefficient h is calculated by using the natural convection correlation from [24]. The cavity wall temperature $T_w(t)$ was measured experimentally by using sample #1. The above discussed agreement between the calculated and measured temperatures of the sample and ceramic tube surface confirms that the coefficients used in the boundary conditions (18) and (19) are correct.

5.3. Determination of the temperature field by using the measured boundary temperature

Sample #2 was used in a reference experimental run conducted at moderate incident solar flux, $q_s = 0.91$ MW m^{-2}, which enabled long-time heating without a significant mass decrease of the front ZnO plate (approximately 4.2%). The boundary condition of the first kind at the surface S is applied, i.e. the measured temperature of the irradiated surface T_s shown in Fig. 6 is used as a boundary condition. The thermal conductivity of the plates is set to $k_1 = 2$ W m^{-1} K^{-1}. The emissivity of the ceramic insulation is set to $\varepsilon_c = 0.85$. The density of the porous sample varies during the experiment with concurrent formation of gaps (see Fig. 7), but the total mass of this sample remains constant during the experiment. Thus, the average density in the volume occupied by this sample, $\rho = 1671$ kg m^{-3}, is used to calculate the average volumetric heat capacity. The effective thermal conductivity of the porous sample is expected to increase with temperature due to the contribution by thermal radiation, grain growth, and sintering. For simplicity, it is assumed that it increases linearly from 1 to 10 W m^{-1} K^{-1} between 300 and 2300 K. The results shown in Fig. 6 indicate good agreement between the calculated and measured values of T_{p_1}. The small increase of measured T_{p_1} is explained by the ablation of the surface layer. The more pronounced increase of T_{p_2} and T_c with time results from the time variation of the

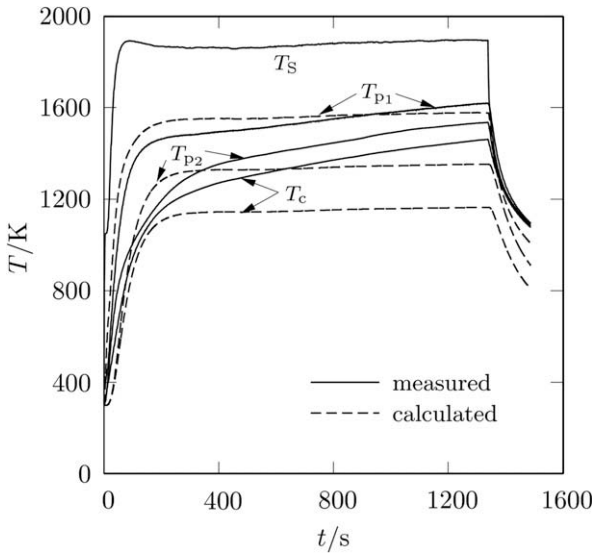

Fig. 6. Comparison of the measured and calculated temperatures in the composite sample for the reference experimental run.

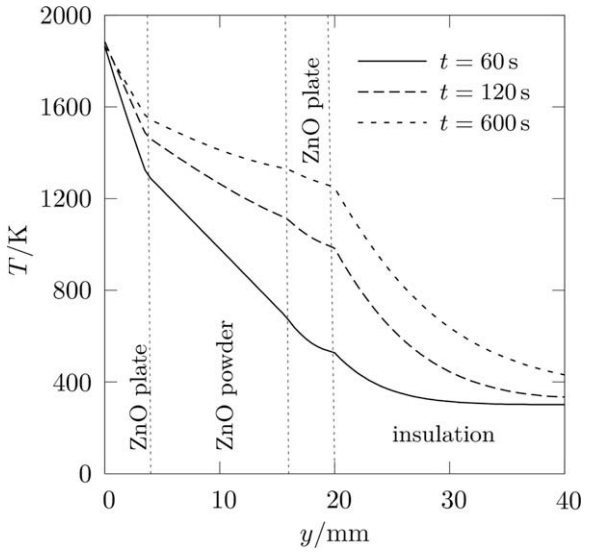

Fig. 8. Numerically calculated temperature profiles along the axis of the composite sample in the reference experimental run.

physical properties of the porous layer. Fig. 7a and b show the sintered ZnO plate and the porous ZnO layer after the experiment, respectively. Due to the sintering, a large circular gap between the sample and the insulation tube is formed. Sintering justifies using an increasing thermal conductivity – for which a better agreement between the measured and calculated temperatures is obtained.

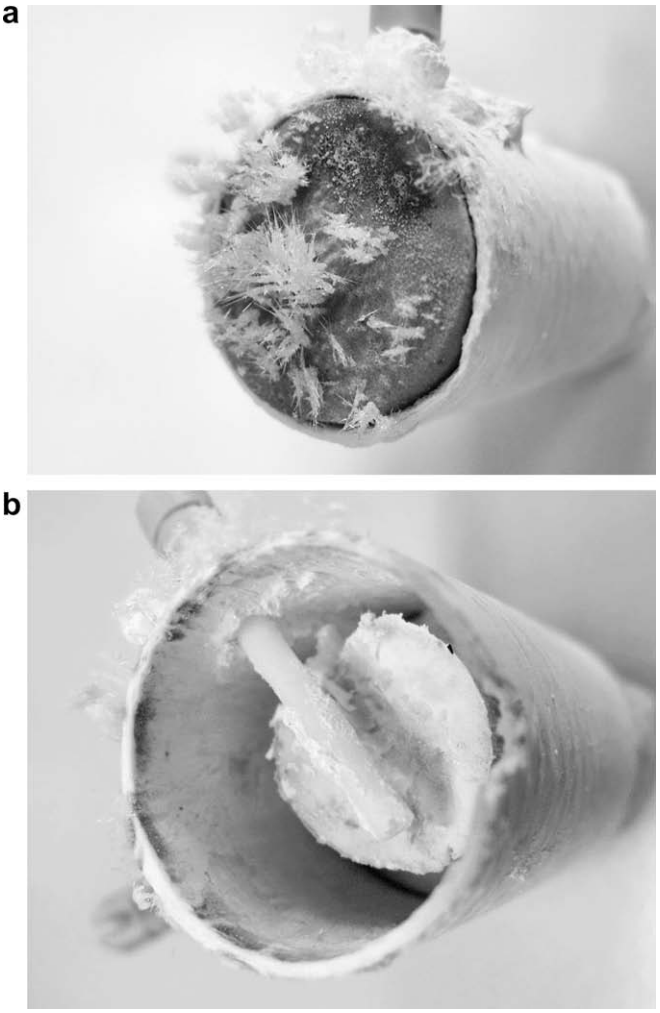

Fig. 7. Photographs taken after the reference experimental run: (a) sintered front plate, and (b) porous sample after removing the front plate.

The calculated axial temperature profiles are shown in Fig. 8. These are approximately linear in each ZnO layer and enable a simplified engineering approach. Specifically, the conductive heat flux from the ablating surface can be easily estimated by using the temperature difference in the front plate. The conductive heat flux was found to be approximately equal to 0.2 MW m^{-2}.

5.4. Determination of the temperature field by using the radiation–convection boundary condition

In the present section, the boundary condition (18) is employed to determine the temperature field. Since the mass loss rate is strongly dependent on T_s, this temperature should be determined with maximum accuracy. For this purpose, the experimental data obtained during the reference experimental run with sample #2 are used. The energy balance at the sample surface during the quasi-steady period is formulated as:

$$\alpha_s q_s = \varepsilon_s \sigma \left(T_s^4 - T_w^4 \right) + q_{cond} + q_{conv} + \Delta H \cdot K \exp\left(-E/RT_s\right) \qquad (32)$$

where all the terms are practically independent of time. Note that $T_w^4 << T_s^4$ and the corresponding term in Eq. (32) can be simplified. For the conditions of the reference experimental run, the last term in Eq. (32) is also negligible and can be omitted. The solar radiation, conduction, and convection fluxes are taken equal to $q_s = 0.91$ MW m^{-2}, $q_{cond} = 0.2$ MW m^{-2}, and $q_{conv} = 0.1$ MW m^{-2}, respectively. For $\alpha_s = 0.9$ and $\varepsilon_c = 0.69$ [51], we find $T_s \approx 1900$ K, which is very close to the pyrometer temperature (see Fig. 6). The approach presented in this section leads to the same calculated temperatures inside the sample as those shown in Fig. 6, which confirms the applicability of the boundary condition given by Eq. (18) with the above-specified parameters.

5.5. Determination of the kinetic parameters of ablation

The experimentally measured decomposition rate of ZnO follows an Arrhenius-type law with the surface temperature [15,16]. In our analysis, $E = 361$ kJ/mol [15]. The focus is on the determination of the pre-exponential factor K, which is sensitive

Table 1
Pre-exponential factor in the Arrhenius kinetic law with $E = 361$ kJ/mol.

Sample	Ar flow rate (m^3/s)	K ($kg\,m^{-2}\,s^{-1}$)
#1 using small particles ($F_{v,1}$)	Normal flow rate 0.2×10^{-3}	14.03×10^6
	Double flow rate 0.4×10^{-3}	28.95×10^6
#2 using small particles ($F_{v,1}$)	Normal flow rate 0.2×10^{-3}	8.16×10^6
#2 using large particles ($F_{v,2}$)	Normal flow rate 0.2×10^{-3}	20.36×10^6

to the sample structure (e.g. porosity and particle size) and experimental conditions (e.g. Ar mass flow rate). The corresponding experimental results are presented in Table 1. K strongly increases with the Ar mass flow rate. Interestingly, for the sample containing large particles ($F_{v,2}$), its mass continued to decrease after interruption of the solar irradiation. Note that samples are assumed to be perfectly opaque for incident solar radiation. This assumption appears to be correct for the continuous model of the sample optical properties. However, for porous samples containing large particles, solar radiation may penetrate to depths comparable with the characteristic grain/pore size, leading to a volumetric energy source effect, and consequently, maintain the reaction after interruption of the solar irradiation. A complete model for thermal decomposition of ZnO layers should also include the effect of gas flow over the ablating surface.

6. Conclusions

The thermal decomposition of porous ZnO exposed to concentrated solar radiation can be treated as surface ablation coupled to an Arrhenius-type decomposition rate law. The pre-exponential factor depends significantly on the porosity and grain size of the material, as well as on the mass flow rate of the inert gas. A transient heat transfer model that takes into account combined radiative–conductive heat transfer in a semi-transparent ablating sample is formulated. Both radiative and convective heat losses are included in the boundary conditions. The radiative part of the model is based on the P_1 approximation for the thermal radiation emitted by the sample. The effective thermal conductivity of sintered and porous ZnO is determined by comparing the numerically calculated and experimentally measured temperatures at several locations. The analysis of the temperature field showed that sintering of the porous sample is a long process that takes place even after a quasi-steady temperature field has developed, accompanied by a considerable change in the material effective conductivity. A simplified ablation model based on the surface energy balance and on the estimates of conductive, convective and radiative heat losses is proposed. This model includes a preliminary dependence of the pre-exponential factor on material porosity and convective removal of the gaseous reaction products from the surface. The latter effect, observed experimentally, leads to considerable increase in the decomposition rate.

Acknowledgements

This work has been financially supported by the Swiss National Science Foundation under Contract No. PIOI2-117099, the Russian Foundation for Basic Research under Grant No. 07-08-00015, and the Swiss Federal Office of Energy (SFOE).

References

[1] A. Steinfeld, R. Palumbo, Solar thermochemical process technology, in: R.A. Meyers (Ed.), Encyclopedia of Physical Science and Technology, Academic Press, San Diego, 2001, pp. 237–256.
[2] T. Kodama, High-temperature solar chemistry for converting solar heat to chemical fuels, Prog. Energy Combust. Sci. 29 (6) (2003) 567–597.
[3] A. Meier, E. Bonaldi, G.M. Cella, W. Lipiński, Multi-tube rotary kiln for the industrial solar production of lime, J. Solar Energy Eng. 127 (3) (2005) 386–395.
[4] A. Steinfeld, Solar hydrogen production via a 2-step water-splitting thermochemical cycle based on Zn/ZnO redox reactions, Int. J. Hydrogen Energy 27 (6) (2002) 611–619.
[5] D. Hirsch, A. Steinfeld, Solar hydrogen production by thermal decomposition of natural gas using a vortex-flow reactor, Int. J. Hydrogen Energy 29 (2004) 47–55.
[6] A. Z'Graggen, P. Haueter, D. Trommer, M. Romero, J.C. de Jesus, A. Steinfeld, Hydrogen production by steam-gasification of petroleum coke using concentrated solar power – II. Reactor design, testing, and modeling, Int. J. Hydrogen Energy 31 (6) (2006) 797–811.
[7] C. Perkins, A. Weimer, Likely near-term solar-thermal water splitting technologies, Int. J. Hydrogen Energy 29 (15) (2004) 1587–1599.
[8] P. Haueter, S. Moeller, R. Palumbo, A. Steinfeld, The production of zinc by thermal dissociation of zinc oxide – solar chemical reactor design, Solar Energy 67 (1–3) (1999) 161–167.
[9] R. Müller, P. Haeberling, R.D. Palumbo, Further advances toward the development of a direct heating solar thermal chemical reactor for the thermal dissociation of ZnO(s), Solar Energy 80 (5) (2006) 500–511.
[10] R. Palumbo, M. Keunecke, S. Möller, A. Steinfeld, Reflections on the design of solar thermal chemical reactors: thoughts in transformation, Energy 29 (5–6) (2004) 727–744.
[11] E.A. Secco, Decomposition of zinc oxide, Can. J. Chem. 38 (1960) 596–601.
[12] W. Hirschwald, F. Stolze, Kinetics of the thermal dissociation of zinc oxide, Z. Phys. Chem. Neue Folge 77 (1972) 21–42.
[13] K. Koumoto, H. Yanagida, S. Mizuta, Evaporation of zinc oxide from spinel solid solutions in vacuum, J. Am. Ceram. Soc. 63 (1–2) (1980) 17–20.
[14] S. Möller, R. Palumbo, Solar thermal decomposition kinetics of ZnO in the temperature range 1950–2400 K, Chem. Eng. Sci. 56 (15) (2001) 4505–4515.
[15] L.O. Schunk, A. Steinfeld, Kinetics of the thermal dissociation of ZnO exposed to concentrated solar irradiation using a solar-driven thermogravimeter in the 1800–2100 K range, AIChE J., in press.
[16] L.O. Schunk, W. Lipiński, A. Steinfeld, Ablative heat transfer in a shrinking packed-bed of ZnO undergoing solar thermal dissociation, AIChE J., in press.
[17] P. Haueter, T. Seitz, A. Steinfeld, A new high-flux solar furnace for high temperature thermochemical research, J. Sol. Energy Eng. 121 (1999) 77–80.
[18] J.M. Cowley, A.L.G. Rees, J.A. Spink, The morphology of zinc oxide smoke particles, P. Phys. Soc. Lond. B64 (1951) 638–644.
[19] A. Weidenkaff, A. Steinfeld, A. Wokaun, P.O. Auer, B. Eichler, A. Reller, Direct solar thermal dissociation of zinc oxide: condensation and crystallisation of zinc in the presence of oxygen, Solar Energy 65 (1999) 59–69.
[20] A. Weidenkaff, A. Reller, F. Sibieude, A. Wokaun, A. Steinfeld, Experimental investigations on the crystallization of zinc by direct irradiation of zinc oxide in a solar furnace, Chem. Mater. 12 (2000) 2175–2181.
[21] R. Mueller, A. Steinfeld, H_2O-splitting thermochemical cycle based on ZnO/Zn-redox: quenching the effluents from the ZnO dissociation, Chem. Eng. Sci. 63 (2008) 217–227.
[22] L.A. Dombrovsky, Radiation Heat Transfer in Disperse Systems, Begell House, New York, 1996.
[23] M.F. Modest, Radiative Heat Transfer, second ed., Academic Press, New York, 2003.
[24] S.W. Churchill, H.H.S. Chu, Correlating equations for laminar and turbulent free convection from a horizontal cylinder, Int. J. Heat Mass Transfer 18 (9) (1975) 1049–1053.
[25] M. Binnewies, E. Milke, Thermochemical Data of Elements and Compounds, second ed., Wiley-VCH, Weinheim, 2002.
[26] Y.S. Touloukian, R.W. Powell, C.Y. Ho, P.G. Klemens, Thermophysical properties of matter, vol. 2, Thermal Conductivity, Nonmetallic Solids, IFI/Plenum, New York, Washington, 1970.
[27] K.F. Cai, E. Müller, C. Drašar, A. Mrotzek, Preparation ant thermoelectric properties of Al-doped ZnO ceramics, Mater. Sci. Egn. B 104 (1–2) (2003) 45–48.
[28] T. Olorunyolemi, A. Birnboim, Y. Carmel, O.C. Wilson Jr., I.K. Lloyd, Thermal conductivity of zinc oxide: from green to sintered state, J. Am. Ceram. Soc. 85 (5) (2002) 1249–1253.
[29] W.L. Bond, Measurement of refractive indices of several crystals, J. Appl. Phys. 36 (5) (1965) 1674–1677.
[30] Y.S. Park, J.R. Schneider, Index of refraction of ZnO, J. Appl. Phys. 39 (7) (1968) 3049–3052.
[31] H. Yoshikawa, S. Adachi, Optical constants of ZnO, Jpn. J. Appl. Phys. 36 (10) (1997) 6237–6243.
[32] G. Ghosh, Handbook on thermo-optic coefficients of optical materials with applications, Academic Press, San Diego, 1998.
[33] L.A. Dombrovsky, W. Lipiński, A. Steinfeld, A diffusion-based approximate model for radiation heat transfer in a solar thermochemical reactor, J. Quant. Spectr. Radiat. Transfer 103 (3) (2007) 601–610.
[34] L.A. Dombrovsky, W. Lipiński, Transient temperature and thermal stress profiles in semi-transparent particles under high-flux irradiation, Int. J. Heat Mass Transfer 50 (11–12) (2007) 2117–2123.
[35] S. Tolksdorf, Untersuchung der ultraroten Eigenschwingungen binären Oxyde (BeO, MgO, CaO, ZnO), Z. Phys. Chem. 132 (1928) 161–184.

[36] G. Bogner, E. Mollwo, Über die Herstellung von Zinkoxydeinkristallen mit definierten Zusätzen, J. Phys. Chem. Solids 6 (2–3) (1958) 136–143.
[37] D.G. Thomas, Infrared absorption in zinc oxide crystals, J. Phys. Chem. Solids 10 (1) (1959) 47–51.
[38] A. Mosbah, A. Moustaghfir, S. Abed, N. Bouhssira, M.S. Aida, E. Tomasella, M. Jacquet, Comparison of the structural and optical properties of zinc oxide thin films deposited by d.c. and r.f. sputtering and spray pyrolysis, Surf. Coat. Technol. 200 (1–4) (2005) 293–296.
[39] B.M. Keyes, L.M. Gedvilas, X. Li, T.J. Coutts, Infrared spectroscopy of polycrystalline ZnO and ZnO:N thin films, J. Crystal Growth 281 (2–4) (2005) 297–302.
[40] S. Shirakata, T. Sakemi, K. Awai, T. Yamamoto, Electrical and optical properties of large area Ga-doped ZnO thin films prepared by reactive plasma deposition, Superlatt. Microstr. 39 (1–4) (2006) 218–228.
[41] M. Tancrez, J. Taine, Direct identification of absorption and scattering coefficients and phase function of a porous medium by a Monte Carlo technique, Int. J. Heat Mass Transfer 47 (2004) 373–383.
[42] J. Petrasch, P. Wyss, A. Steinfeld, Tomography-based Monte Carlo determination of radiative properties of reticulate porous ceramics, J. Quant. Spectrosc. Radiat. Transfer 105 (2) (2007) 180–197.
[43] D. Baillis, J.-F. Sacadura, Thermal radiation properties of dispersed media: theoretical prediction and experimental characterization, J. Quant. Spectrosc. Radiat. Transfer 67 (5) (2000) 327–363.
[44] L. Dombrovsky, J. Randrianalisoa, D. Baillis, L. Pilon, Use of Mie theory to analyze experimental data to identify infrared properties of fused quartz containing bubbles, Appl. Opt. 44 (33) (2005) 7021–7031.
[45] L. Dombrovsky, J. Randrianalisoa, D. Baillis, Modified two-flux approximation for identification of radiative properties of absorbing and scattering media from directional-hemispherical measurements, J. Opt. Soc. Am. A 23 (1) (2006) 91–98.
[46] L.A. Dombrovsky, H.K. Tagne, D. Baillis, L. Gremillard, Near-infrared radiative properties of porous zirconia ceramics, Infrared Phys. Technol. 51 (1) (2007) 44–53.
[47] B.P. Singh, M. Kaviany, Independent theory versus direct simulation of radiation heat transfer in packed beds, Int. J. Heat Mass Transfer 34 (11) (1991) 2869–2882.
[48] B.P. Singh, M. Kaviany, Modelling radiative heat transfer in packed beds, Int. J. Heat Mass Transfer 35 (6) (1992) 1397–1405.
[49] Q. Brewster, Volume scattering of radiation in packed beds of large, opaque spheres, ASME J. Heat Transfer 126 (4) (2004) 1048–1050.
[50] R. Coquard, D. Baillis, Radiative characteristics of opaque spherical particles beds: a new method of prediction, AIAA J. Thermophys. Heat Transfer 18 (2) (2004) 178–186.
[51] S. Möller, Entwicklung eines Reaktors zur solarthermischen Herstellung von Zink aus Zinkoxid zur Energiespeicherung mit Hilfe konzentrierter Sonnenstrahlung, Ph.D. thesis, ETH Zürich, 2001.